Emulsification with rectangular tubes

Erwan Crestel, Ladislav Derzsi, Hugo Bartolomei, Jérôme Bibette, and Nicolas Bremond*
Institute of Chemistry, Biology and Innovation, UMR8231, CNRS, ESPCI Paris, PSL Research University, 10 Rue Vauquelin, 75005 Paris, France*

(Received 15 January 2019; published 19 July 2019)

The flow of two immiscible liquids or fluids in bounded systems where confinement geometry varies can lead to drop or bubble formation. This phenomenon has been reported in the context of oil recovery and named snap-off, or exploited for making emulsions, and then foams, by using microfluidic systems, namely, microchannel emulsification or step emulsification. We report a comprehensive experimental investigation of such an emulsification process occurring at the end of a glass rectangular tube filled with oil and immersed in a water bath. This allows us to clearly visualize the breakup event of the dispersed phase liquid finger at the capillary's end. Below a critical flow rate, the drop size varies slowly with the flow rate and it is linked to the pinching time of the dispersed phase. A semiempirical law that gives the resulting drop size as a function of fluid and geometrical properties is proposed. However, this feature is altered for an aspect ratio of the rectangular tube below 2.5 where the forming drop hinders the counterflow of the continuous phase leading to larger drops. Then, above a critical flow rate, or capillary number that weakly depends on the viscosity ratio of the two liquids, the neck adopts a quasistatic shape well accounted for by a model based on a Hele-Shaw flow. In that case, drop formation is driven by gravity and a transition from a dripping regime to a jetting regime is observed at higher flow rates. Monodisperse foam can also be formed by injecting air. While the overall dynamics of bubble formation shares similarities with an incompressible fluid, the bubble size and the critical capillary number do not follow the same scaling laws.

DOI: 10.1103/PhysRevFluids.4.073602

I. INTRODUCTION

Surface-tension-driven flows are ubiquitous in nature [1]. Flows may be induced by surface-tension gradient, so-called Marangoni flows, with the famous example of wine tears [2]. Liquid motion is also induced by capillary pressure gradient linked to interface curvature inhomogeneity, where surface tension may be also time and scale dependent. Such phenomena play a major role in liquid fragmentation, from atomization to emulsification [3]. Bounded multiphase flows experience liquid breakup, like in a porous medium in the context of oil recovery applications [4,5]. The interfacial curvature is imposed by the geometrical confinement of the pore throat that may lead to capillary pressure imbalance and finally the snap-off of water immersed in oil, or vice versa. This phenomenon has been exploited in the context of emulsification where the dispersed phase is pushed through a porous medium immersed in a second immiscible phase, namely, membrane emulsification [6–8]. Here the pores exhibits an elongated shape and the drop size distribution is linked to the variation of pore geometry. The development of microfabrication technologies led to a precise manufacture of regular arrays of microchannels having a trapezoidal or rectangular shape, mimicking pore structure while leading to homogeneous droplet size [9,10]. This method

*nicolas.bremond@espci.fr

TABLE I. Properties of the dispersed phases at 25 °C where γ is the interfacial tension between the oils and an aqueous solution of SDS at 1 wt.% excepted for FC40a where the aqueous phase is free of surfactant. The value of γ for SO10 has been extrapolated from the necking time (see the text for details).

Dispersed phase	η_i (mPa s)	ρ_i (kg/m^3)	γ (mN/m)
	Fluorocarbon oils		
FC-3283	1.4	1820	18.8
FC-40	4.1	1850	18.8
FC-40a	4.1	1850	50.5
FC-70	24	1940	19.4
	Silicon oils		
SO5	4.6	960	10.4
SO10	10	1000	12.0
SO20	20	950	12.0
SO50	48	960	11.0
SO100	96.5	965	11.7
SO100a	106	1006	9.2
SO500	485	960	12.0
SO1000	970	970	12.0
	Air		
	0.018	1.18	35

for producing emulsions is known as microchannel emulsification or step emulsification. Since then, various modifications have been implemented, including a straight-through geometry [11], a coflow of the continuous phase [12,13], a variation of the microchannel's height [14] and width [15] including a diverging shape [16] and even shunt channels [17]. Such a method is also well suited for making monodisperse foams [18].

This strategy of emulsification offers a unique way to produce a large number of homogeneous droplets. First, below a critical flow rate of the dispersed phase, droplet size is mainly linked to the microchannel geometry and thus to their manufacturing quality [19]. Second, it is straightforward to parallelize microchannels for enhancing the throughput [20]. Calibrated emulsion droplets find various applications as they can act as chemical reactors or bioreactors where molecules or cells are encapsulated [21] or they can be used to create functional particles [22].

Here we study the drop formation that occurs at the end of a glass capillary having a rectangular cross section. After introducing the materials and methods used in this work, the features of the drop formation dynamics as a function of fluid properties are reported. The influence of the capillary geometry, including the aspect ratio, is also investigated. These features include the characteristic timescale of drop formation, the drop size, and the critical flow rate above which the snap-off solely driven by surface tension is stopped. A model of the quasistatic shape of the neck above the transition is then detailed. The peculiar dynamics of bubble formation for which gas compressibility comes into play is finally studied.

II. MATERIALS AND METHODS

The continuous aqueous phases are prepared from ultrapure water (Milli-Q). A surfactant, sodium dodecyl sulfate (SDS) (Sigma-Aldrich), is used at a concentration of 1 wt.%. The viscosity of the continuous phase η_0 is tuned by adding a low-molecular-weight polymer, polyethylene glycol (PEG 3350) (Sigma-Aldrich), at various concentrations up to 35 wt.% that corresponds to η_0 equal to 26 mPa s at 25 °C [23]. The dispersed phase is either fluorocarbon oil (3M Fluorinert), silicone oil (Dow Corning) purchased from Sigma-Aldrich, or air. Their bulk properties are reported in Table I. The corresponding interfacial tension γ with the aqueous solution of SDS at a concentration

FIG. 1. Front view of a rectangular glass capillary having a height h of 96 μm and a width w of 1050 μm.

above the critical micellar concentration is given in Table I. The interfacial tension is measured by the pending drop technique (SA100, Krüss). We note that, contrary to other microfluidic techniques [24], the wetting of the dispersed phase onto the confining walls should be limited as it can induce a failure of the emulsification process [25,26]. Therefore, choosing the right surfactant and/or modifying the wall properties is a crucial step for using such an emulsification process [27]. Here the glass capillaries are initially cleaned with an oxygen plasma cleaner (FEMTO, Diener electronic), leading to a complete wetting of water on the glass wall in the presence of SDS (see Fig. S1 in Ref. [28]).

The rectangular glass capillaries are purchased from Vitrocom. The height h varies from 20 μm to 200 μm and the width w from 200 μm to 2000 μm, with an aspect ratio w/h of about 10 or 20. They are diced with the help of a ceramic cleaving stone (Polymicro Technologies). A snapshot of a capillary cross section is shown in Fig. 1. The walls are not perfectly parallel and may vary from capillary to capillary. For smaller aspect ratios, a channel is made by gluing glass plates having a thickness of 1 mm. Once selected, the glass capillary is glued on a glass plate by keeping one extremity outside the plate. The other extremity is used for infusing the phase to be dispersed by gluing a syringe needle that fits into a plastic tube connected to a glass syringe. The flow is then controlled with the help of a syringe pump (PhD Ultra, Harvard Apparatus). The glass plate is held above a square glass cuvette filled with the continuous phase with a three-way microcontrol stage. The tip of the glass capillary is then immersed in the water bath and illuminated with a light-emitting-diode panel (SLLUB backlight, Phlox). The dynamics of drop formation is observed with a high-speed camera (FastCam SA3, Photron) mounted on a macrozoom microscope (MVX10, Olympus) set horizontally. Alternatively, the whole glass plate is immersed in a larger cuvette so that the rectangular tube's extremity points upward. We did not notice any modification of the droplet formation dynamics in such a configuration.

III. RESULTS AND DISCUSSION

A time sequence of drop formation at a capillary's end seen from both sides is shown in Fig. 2(a) (see also movie S1 in Ref. [28]). From these images, the radii of curvature r_{xy} and r_{xz} at the apex of the liquid finger in the planes $\{x, y\}$ and $\{x, z\}$ can be measured. They are reported in Fig. 2(d) as a function of time. Before reaching the capillary's extremity, the shape of the fingertip is nearly circular in both directions, the radii being mainly imposed by the channel geometry with a correction due to the viscous flow [29]. As revealed on the spatiotemporal diagram shown in Fig. 2(b), the corresponding trajectory of the fingertip is initially straight, i.e., the apex travels at a constant velocity. Then, at a distance from the edge of the order of the capillary's height and reached at a time denoted by t_s, the fingertip accelerates. The sign of the curvature $\mathcal{C}_{xy}$ of the meniscus in the $\{x, y\}$ plane is inverted at a location close to the edge; a necking phase is taking place. As revealed by the spatiotemporal diagram in the y direction at the location of the neck breakup [Fig. 2(c)], the neck's width decreases for $t > t_s$, seems to reach a plateau, and finally collapses in a few milliseconds when the width is of the order of the channel's height. The overall dynamics shares similarities with other microfluidics situations where the vertical confinement leads to a two-dimensional collapse [30], stability against perturbation of the interface [31], and a final three-dimensional stage of the neck breakup ruled by the classical Rayleigh-Plateau instability [3]. The confinement release triggers the pinch-off of the fingertip. Indeed, in a quasistatic approach, where the variations of liquid

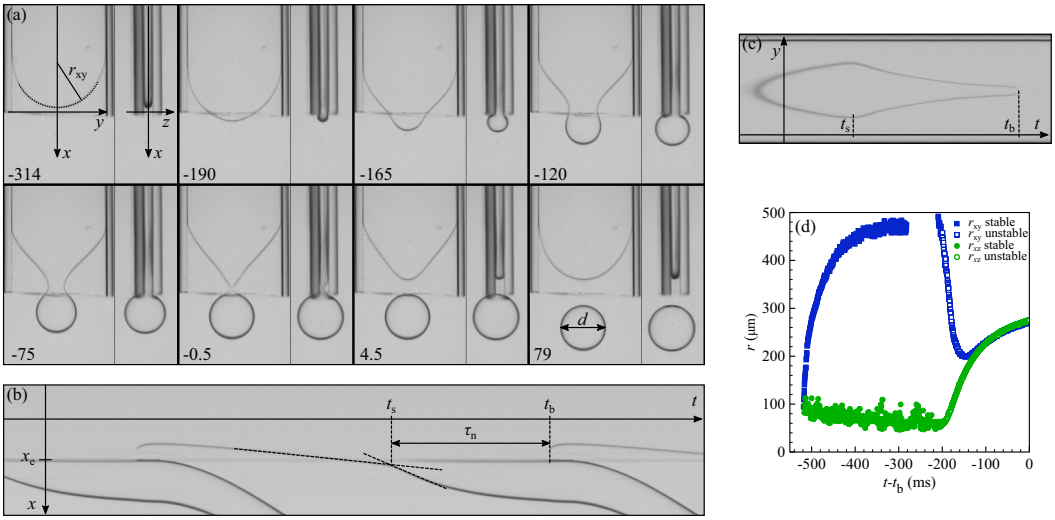

FIG. 2. (a) Time sequence showing the drop formation from a rectangular glass capillary observed from both sides ($w = 1000$ μm and $h = 100$ μm). Time is indicated in milliseconds and $t = 0$ matches the time when the neck breaks up. Gravity is pointing downward, in the x direction. (b) Spatiotemporal diagram in the x direction in the midline of the channel from which characteristic timescales of drop formation are evaluated. (c) Spatiotemporal diagram in the y direction at the location of the neck breakup. (d) Time evolution of the radii of curvature r_{xy} and r_{xz} evaluated during a period of drop formation, the reference time being taken at breakup, i.e., at t_b. The time period when the meniscus is stable is indicated by closed symbols and the unstable phase by open ones.

pressure due to the viscous flow are neglected, the mean curvature of the meniscus $\mathcal{C} = \mathcal{C}_{xy} + \mathcal{C}_{xz}$ is constant [32]. When the finger's apex is out of the rectangular tube, the interface can now expand in the z direction, leading to an increase of r_{xz} and thus a decrease of $\mathcal{C}_{xz}$. This phase is called unstable in Fig. 2(d). On the other hand, the radius in the other plane, r_{xy}, first decreases, then increases, and becomes equal to r_{xz}. An inflating drop connected to the liquid finger is thus formed. As discussed later on, the pressure drop in the neck due to viscous flow is not high enough to balance the variation of the capillary pressure induced by the modification of the interfacial curvature. As a consequence, the neck continues to shrink and finally breaks up at a time t_b. One can then define a necking time $\tau_n = t_b - t_s$. The necking phase results in the formation of a drop having a diameter d. Then the meniscus shape relaxes to a quasicircular shape before being pushed again towards the capillary extremity where the emulsification process is repeated.

Let us now discuss in more detail how the channel geometry and the liquid properties impact on such an emulsification process. The evolution of the drop size along with the necking time are first reported in Fig. 3(a) as a function of the flow rate of a silicone oil (SO5). The glass capillary has a height of 50 μm and has a width ten times larger. The drop size is initially constant and equal to $d_0 = 220$ μm up to $q = 100$ μl/h. Then d increases and reaches a value of about 250 μm at $q = 500$ μl/h. The neck is stabilized above this flow rate as discussed later on. The corresponding necking time is almost constant; it decreases from 30 ms to 25 ms over the whole range of flow rates. The dependence of drop size on the flow rate can then be evaluated from an inflation mechanism where the volume of the drop $V = \pi d^3/6$ is equal to a minimal volume $V_0 = \pi d_0^3/6$ plus the volume injected at a flow rate q during a time τ_0 proportional to τ_n. This leads to an estimation of the drop size as

$$d = d_0\left(1 + \frac{6q\tau_0}{\pi d_0^3}\right)^{1/3}. \tag{1}$$

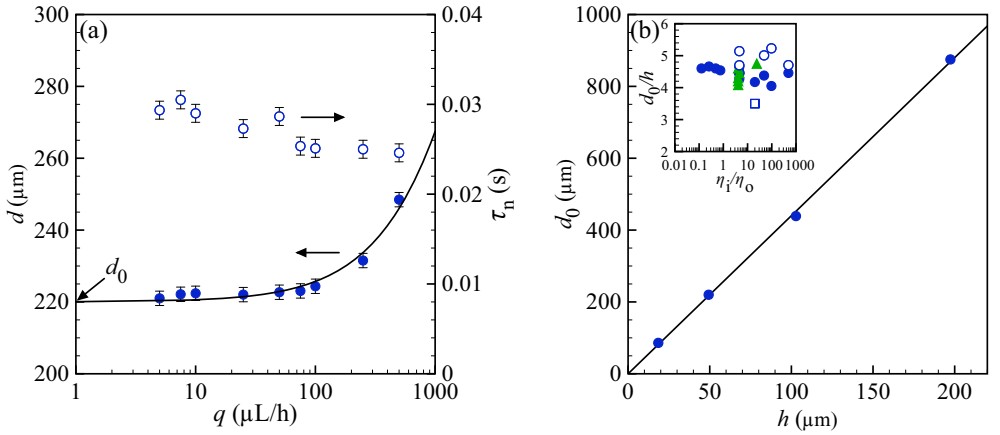

FIG. 3. (a) Evolution of the drop diameter d (•) and the necking time τ_n (○) as a function of the flow rate. The height of the capillary is 50 μm, the width is 500 μm, and the dispersed phase is the silicone oil SO5. The solid line corresponds to Eq. (1). (b) Variation of the drop size d_0 with the height h of the capillary. The dispersed phase is the silicone oil SO5. The solid line is a purely linear fit with a slope of 4.4. The inset shows the drop size normalized by the capillary height as a function of the viscosity ratio η_i/η_o for silicone oils with capillaries having an aspect ratio w/h equal to 2 (□), 11 (•), and 20 (○) and fluorocarbon oils with $w/h = 11$ (▲).

The evolution of d given by Eq. (1) correctly predicts the experimental data, as shown in Fig. 3(a), once the characteristic size d_0 and timescale τ_0 are adjusted. Here τ_0 is equal to 16 ms, which is a bit more than half the average value of τ_n.

As reported in Fig. 3(b), the minimal drop size d_0 is proportional to the tube's height h and, for $w/h \sim 10$, is given by $d_0 = 4.4h$. The drop size d_0 is independent of the viscosity of both phases and the interfacial tension as shown in the inset of Fig. 3(b). The overall data at this aspect ratio, which is 10.8 ± 0.3, give a drop size $d_0 = (4.5 \pm 0.2)h$. We note that we did not find a marked increase of d_0 for low viscosity ratios as observed earlier [33]. On the other hand, as reported in the inset of Fig. 3(b), d_0 slightly depends on the tube's width. The drop size is indeed about five times the tube's height when $w/h = 20$. This is in accordance with the influence of the flow rate ratio for a coflow situation [34]. Even though the aspect ratio is not varied over a wide range, the relationship between drop size and tube geometry can be estimated,

$$d_0 = h\left(3.9 + 0.05\frac{w}{h}\right). \tag{2}$$

As discussed in a previous investigation [19], the characteristic timescale of drop formation τ_0 is a function of channel geometry and fluid properties. As reported in Fig. 4, τ_0 is a purely linear function of the inner phase viscosity η_i. The coefficient of proportionality increases with the aspect ratio w/h [Fig. 4(a)]. In addition, it is a linear function of the outer viscosity η_o [Fig. 4(b)]. Since the necking phase is driven by the interfacial tension, τ_0 is found to be inversely proportional to γ [Fig. 4(c)]. Finally, we note that τ_0 increases linearly with the tube's height h [Fig. 4(d)]. The necking dynamics is solely ruled by a competition between interfacial tension and viscous dissipation linked to the confinement geometry. The characteristic timescale of the necking process is empirically found to be proportional to a time defined by a capillary velocity γ/η_i and a characteristic length scale h corrected by the viscosity ratio and the aspect ratio as

$$\tau_0 = a\left(1 + \alpha\frac{\eta_o}{\eta_i}\right)\left(1 + \beta\frac{w}{h}\right)\frac{\eta_i h}{\gamma}. \tag{3}$$

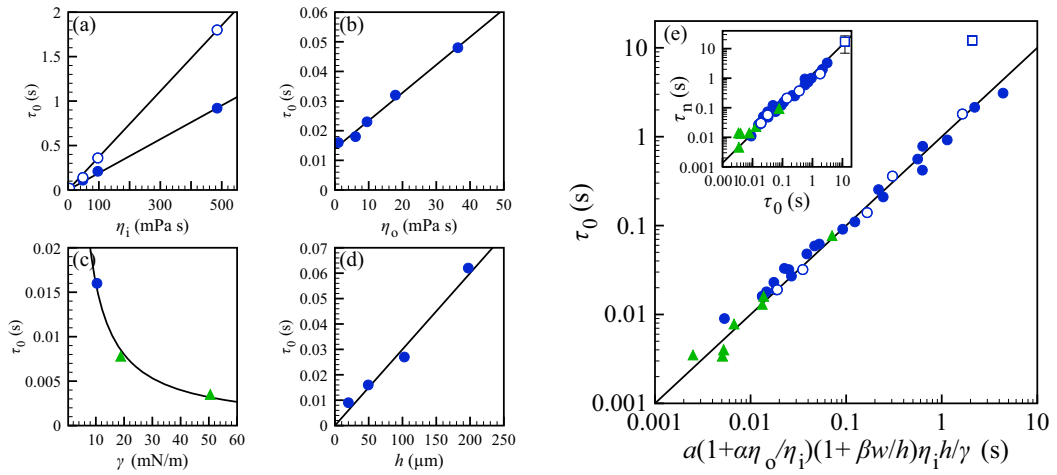

FIG. 4. Characteristic timescale of drop formation τ_0 as a function of (a) the inner viscosity η_i for two aspect ratios w/h equal to 11 (•) and 20 (○) with $\eta_o = 1$ mPa s and $h = 50$ μm, (b) the outer viscosity with $\eta_i = 4.65$ mPa s and $h = 50$ μm, (c) the interfacial tension γ for silicon oil (•) and fluorocarbon oil (▲) with $h = 50$ μm, and (d) the height h with $\eta_i = 4.65$ mPa s and $\eta_o = 1$ mPa s. The solid lines represent linear functions or are proportional to $1/\gamma$ in (c). (e) Characteristic timescale τ_0 versus the empirical scaling law where $a = 375$, $\alpha = 4.7\times10^{-2}$, and $\beta = 0.33$. The symbols represent data sets with the same fluid properties and tube geometry as in Fig. 3(b). The solid line is a purely linear function with a prefactor of 1. The inset shows correlation between the average necking time τ_n and τ_0. The solid line is a purely linear fit with a prefactor of 1.36.

The constants a, α, and β are adjusted to 375, 0.047, and 0.33, respectively [Fig. 4(e)]. We note that a point does not collapse onto the master curve in Fig. 4(e). This value of τ_0 corresponds to a rectangular channel having an aspect ratio of 2. The experimental necking time is longer than the empirical value given by Eq. (3). This discrepancy is discussed in the next paragraph. The correlation between τ_0 and the necking time as defined in Fig. 2(b) is also reported in Fig. 4(e). Both times are proportional with a coefficient of proportionality equal to 1.36, whatever the aspect ratio. By combining Eqs. (1)–(3), we finally end up with a semiempirical law for the drop size as a function of the flow rate, the liquid properties, and the tube dimensions,

$$\frac{d}{h} = \left(3.9 + 0.05\frac{w}{h}\right)\left[1 + \frac{6aq\eta_i}{\pi\left(3.9 + 0.05\frac{w}{h}\right)^3\gamma h^2}\left(1 + \alpha\frac{\eta_o}{\eta_i}\right)\left(1 + \beta\frac{w}{h}\right)\right]^{1/3}. \tag{4}$$

The influence of the aspect ratio on the necking dynamics is reported in Fig. 5(a). The necking time is almost constant for large w/h and grows below a critical ratio of 2.5. Two snapshots of the neck before breakup are also shown for w/h equal to 2 and 4. We notice that the location of the neck pinch-off is close to the step for a ratio larger than the critical one and further upstream for a smaller aspect ratio. In that case, when necking takes place, the drop is larger than the channel's width. The drop hinders the counterflow of the continuous phase and thus delays the collapse dynamics of the neck. Necking will be induced as soon as there is a curvature gradient [32], which is always the case at the extremity of a rectangular channel whatever the aspect ratio. This has also been recently verified for a round capillary [35,36]. According to Eq. (1), this delay has a direct impact on the resulting drop size. To compare two aspect ratios, the drop size normalized by the minimal drop size d_0 is plotted in Fig. 5(b) against the flow rate divided by the critical flow rate q_c above which larger drops are formed. The link between q_c and τ_0 is discussed below. The normalized drop size

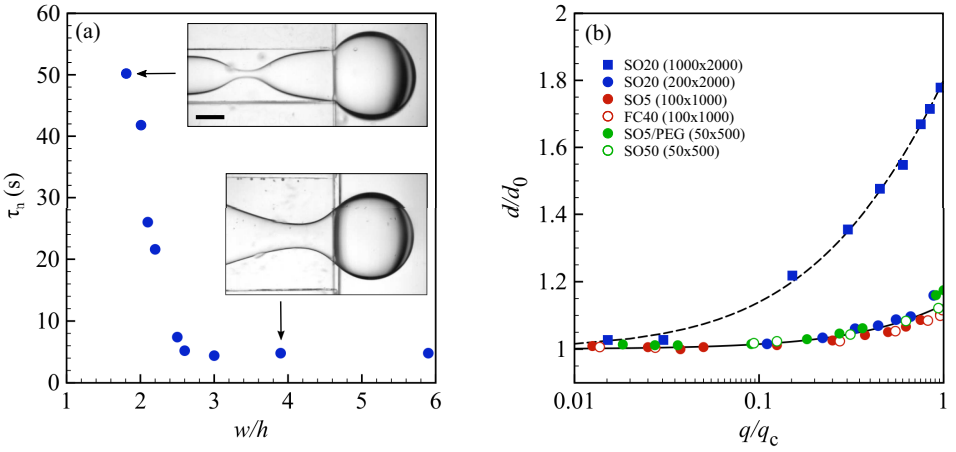

FIG. 5. (a) Evolution of the necking time τ_n as a function of the aspect ratio h/w for SO20 along with two snapshots prior to breakup. The scale bar is 1 mm. (b) Growth of the normalized drop size d/d_0 as a function of the flow rate ratio q divided by the critical flow rate ratio q_c at the transition for two aspect ratios, 2 (squares) and 10 (circles), and various formulation and capillary geometries. The width and the height of the rectangular capillaries are indicated in micrometers in the legend. The lines correspond to Eq. (5) for b equal to 0.45 (solid line) and 4.8 (dashed line).

is now given by

$$\frac{d}{d_0} = \left(1 + b\frac{q}{q_c}\right)^{1/3}, \tag{5}$$

where the constant b is equal to 0.45 for $w/h = 10$ and to 4.8 for $w/h = 2$. It is therefore advantageous to work with an aspect ratio larger than 2.5 to limit the influence of the flow rate on the resulting drop size (4). Interestingly, all the data obtained for various fluid properties collapse on a single curve. This indicates a direct relationship between the critical flow rate and the characteristic timescale of drop formation as previously suggested [19]. This correlation is reported in Fig. 6(a) for all the experimental conditions. The critical flow rate q_c is proportional to the flow rate created by d_0 and τ_0, i.e., $q_c = b\pi d_0^3/6\tau_0$. The constant of proportionality is found to be equal to 0.45 for aspect ratios of 10 and 20. We recall that the data point represented by an open square, which does not gather with the other data, corresponds to an aspect ratio of 2, i.e., below the critical one.

As previously mentioned, the critical flow rate depends on the fluid properties and channel features. The transition occurs at a critical capillary created by the inner phase properties, i.e., $\mathrm{Ca} = \eta_i q/\gamma hw$. As discussed later on, the transition from a small to a large drop formation regime takes place when the viscous pressure drop in the neck is enough to balance the capillary pressure variation linked to the curvature of the interface [34]. The influence of the aspect ratio is recovered by considering the fluid velocity at the neck that has a dimension of the order of h at the transition, i.e., $\mathrm{Ca}^* = \mathrm{Ca}\times(w/h)$. Such a modified capillary number is reported in Fig. 6(a) as a function of the viscosity ratio η_i/η_o. The transition occurs for $\mathrm{Ca}^* = 0.019(\eta_i/\eta_o)^{0.2}$. This behavior suggests that the counterflow of the continuous phase should be taken into account. Streamlines in the continuous phase can be visualized by adding micrometer-size particles in the water. Two examples are shown in Fig. 6(b) when the fingertip is approaching the capillary's end and when the neck is stabilized for a capillary number above the transition. While the flow is initially unidirectional in the rectangular tube, we observe the formation of two vortices beside the meniscus. Such a flow may be at the origin of the slight dependence of the critical capillary number on the viscosity ratio. The description of the meniscus shape beyond the transition of emulsification regime, for a quasisteady shape, is now given by following the analysis of Li *et al.* [34] but without considering a flow of the outer phase.

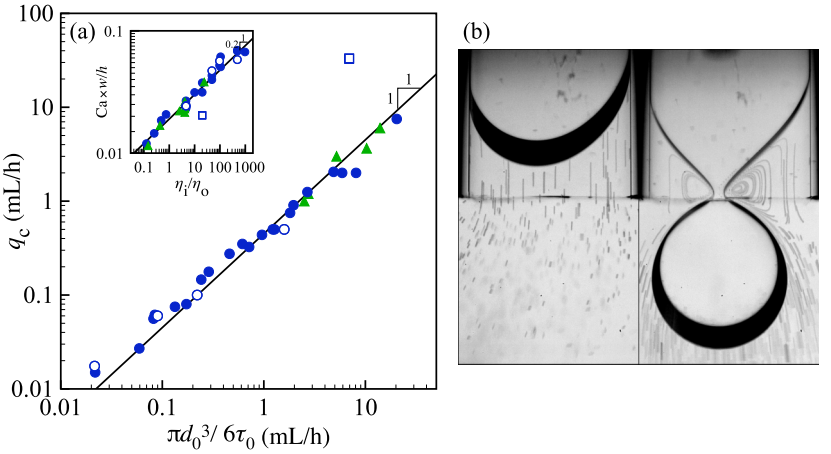

FIG. 6. (a) Correlation between the critical flow rate q_c above which the meniscus is stabilized by the flow and the flow rate created by the characteristic timescale τ_0 and drop size d_0. The solid line is a linear fit with a coefficient of proportionality equal to 0.45. The inset shows the critical capillary number Ca times the aspect ratio of the rectangular tube w/h as a function of the viscosity ratio η_i/η_o. The oblique line corresponds to a power law of 0.2. The symbols represent data sets with the same fluid properties and tube geometry as in Fig. 3(b). (b) Streamlines in the continuous phase revealed by micrometer-size particles when the tip is approaching the tube's end and when the neck is dynamically stabilized. The images are a superposition of 100 snapshots taken every millisecond. The width of the capillary is 1000 μm.

Far from the capillary's end, the flow is assumed to be similar to a Poiseuille flow in a tube having a rectangular cross section $w_m \times h$, where $w_m \sim w$ is the width of the meniscus. When $w_m \gg h$, the flow rate q is given by

$$q = -\frac{h^3 w}{12\eta_i}\frac{dp_i}{dx}, \tag{6}$$

where p_i is the pressure of the inner phase, which is here assumed to depend only on x, i.e., for weak variation of the velocity direction that is principally along x axis. This parallel flow is illustrated in Fig. 6(b) for the outer phase before the meniscus's tip reaches the step location. The inner pressure is linked to the outer pressure p_o through the capillary pressure,

$$p_i(x) = p_o(x) + \gamma\mathcal{C}, \tag{7}$$

where $\mathcal{C}$ is the curvature of the meniscus at a location $\{x, y_m\}$. When $(dy_m/dx)^2 \ll 1$, the curvature is approximated by

$$\mathcal{C} = \frac{2}{h} - \frac{d^2 y_m}{dx^2}. \tag{8}$$

From Fig. 6(b) we clearly see that the quasisteady shape of the meniscus is accompanied by a recirculating flow of the outer phase on each side of the neck. An exact calculation of the pressure field related to this complex flow feature would required numerical simulations. However, for large velocity contrast, i.e., for $\eta_i \gg \eta_o$, one can assume that the viscous pressure drop mainly occurs in the inner phase. Therefore, by letting p_o be constant, the evolution of the meniscus's width is directly linked to the variation of p_i given by Eq. (6). This assumption leads to the following equation for y_m:

$$y_m \frac{d^3 y_m}{dx^3} = \frac{6\eta_i q_i}{\gamma h^3}. \tag{9}$$

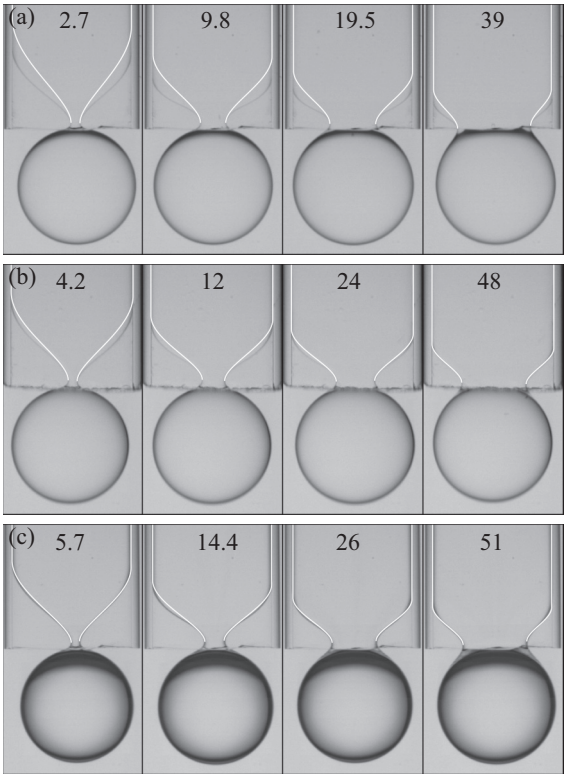

FIG. 7. Quasistatic shapes of the meniscus for increasing flow rates, and thus capillary number Ca, and various viscosities η_i. The value of 10^3Ca is indicated on each picture and η_i is equal to (a) 4.65 mPa s, (b) 48 mPa s, and (c) 106 mPa s. The height and the width of the glass capillaries are about 100 μm and 1000 μm, respectively. The white solid lines are the equilibrium shapes predicted by the integration of Eq. (11).

Using the width w as the characteristic length scale and noting the variables $\tilde{y}_m = y_m/w$ and $\tilde{x} = x/w$, the dimensionless form of Eq. (9) is

$$\tilde{y}_m \frac{d^3\tilde{y}_m}{d\tilde{x}^3} = k, \tag{10}$$

where $k = 6(w/h)^2\text{Ca}$ and $\text{Ca} = \eta_i q_i/wh\gamma$ is the capillary number. The integration of Eq. (10) leads to

$$\tilde{y}_m \frac{d^2\tilde{y}_m}{d\tilde{x}^2} - \frac{1}{2}\left(\frac{d\tilde{y}_m}{d\tilde{x}}\right)^2 = k\tilde{x} + c, \tag{11}$$

where c is a constant of integration. By choosing the location $\tilde{x} = 0$ where $\tilde{y}_m$ reaches its maximum value, i.e., for $\tilde{y}_m = \frac{1}{2}$ and $d\tilde{y}_m/d\tilde{x} = 0$, the constant c is linked to the initial meniscus curvature in the $\{x, y\}$ plane, i.e.,

$$c = \frac{1}{2}\frac{d^2\tilde{y}_m}{d\tilde{x}^2}\bigg|_{\tilde{x}=0}. \tag{12}$$

Numerical resolutions of Eq. (11) are compared in Fig. 7 to experimental meniscus shapes for silicone oils in water for different oil viscosities and at various flow rates, and thus different capillary numbers. The constant c is adjusted such that the minimum of y_m of the theoretical meniscus matches the experimental one. We note that the value of c is an increasing function of Ca. The first

picture for each oil corresponds to the capillary number at the transition from unstable meniscus to quasistatic meniscus. For larger capillary numbers, above the transition, the neck size grows. Meanwhile, the location where the neck breaks is moving downstream, out of the glass capillary. For much larger flow rates, a planar jet is formed and breaks via the growth of propagating capillary waves, like for the dripping to jetting transition at the exit of a cylindrical tube [37] (see movie S1 in Ref. [28]).

For the lowest oil viscosity of 4.65 mPa s [Fig. 7(a)], the model does not properly describe the meniscus shape which is set back from the experimental one, whatever the capillary number. However, for a larger viscosity of 48 mPa s [Fig. 7(b)], the discrepancy is less pronounced and even cancels out for the largest capillary numbers. Then, for an oil viscosity of about 100 mPa s [Fig. 7(b)], the shapes predicted by the model are in good agreement with the observed ones for the whole Ca range. The observed discrepancy for the lowest viscosities might be attributed to the viscous dissipation in the outer phase, and thus to an extra source of pressure drop, which is not taken into account here. For an intermediate oil viscosity, increasing the flow rate reduces the volume occupied by the outer liquid and thus its influence on the pressure. As a consequence, the quasistatic shape of the meniscus is well predicted for higher flow rates [Fig. 7(b)]. The extra pressure drop due to the entrainment flow of the continuous phase [Fig. 6(a)] can be incorporated in an effective viscosity of the inner phase that grows when the outer phase viscosity increases. The static shape of the meniscus for low viscosity ratios is indeed recovered when a higher effective viscosity is used to evaluate the pressure drop in Eq. (6). As a consequence, the transition is reached for a smaller flow rate, or velocity, corresponding to a smaller critical capillary number [Fig. 6(a)]. A more elaborate model would be necessary to predict the exact scaling dependence.

We finally investigate such a phenomenon when the phase to be dispersed is air. A time sequence of bubble formation at the end of a rectangular tube is reported in Fig. 8(a). The overall dynamics shares similarities when oil, an immiscible liquid, is used [Fig. 2(a)], but two main differences are noticed. First, after the necking phase, the fingertip recedes much further upstream. Second, the bubble size is almost as large as the tube's width. As shown in Fig. 8(b), case i, the bubble's diameter is about nine times the capillary's height for low flow rates. The bubble size slightly decreases and reaches a minimum for $q \sim 10$ ml/h and then grows along a similar inflation mechanism as previously discussed. Indeed, for large flow rates, the evolution of d is well described by Eq. (1) but with a characteristic time τ_0 which is almost three times larger than the one predicted by Eq. (3). Also, the necking time τ_n is a weak decreasing function of q and it is here of the order of 4 ms for $h = 100\ \mu$m.

These different features are linked to the compressibility nature of the dispersed phase. Indeed, the volume of air is linked to the pressure that here varies suddenly when the fingertip reaches the capillary's end. Let us make the analogy with a reservoir containing a gas under pressure p_s, here represented by the syringe of volume V_s, that is connected to the external pressure p_e at time $t = 0$ through a tube of length L characterized by a hydrodynamic resistance R_t. The corresponding mass flow rate is [38]

$$\frac{dm}{dt} = -\frac{\rho_g L}{R_t}\frac{dp}{dx}, \tag{13}$$

where m is the mass of gas, ρ_g is the volumetric mass density of gas, and x is the coordinate along the tube's axis. The density depends on the pressure p via the perfect gas law $\rho_g = Mp/\mathcal{R}T$, where M is the gas molar mass, $\mathcal{R}$ the universal gas constant, and T the temperature. The reservoir pressure is thus ruled by

$$\frac{dp_s}{dt} = -\frac{1}{2R_t V_s}\left(p_s^2 - p_e^2\right). \tag{14}$$

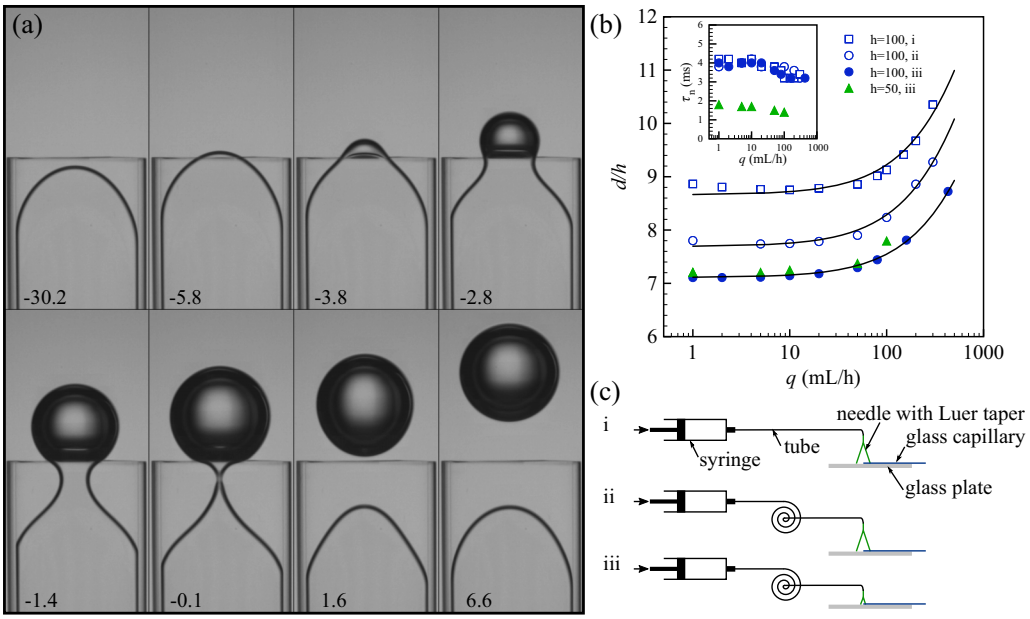

FIG. 8. (a) Time sequence showing the bubble formation from a rectangular glass capillary ($w = 1000\ \mu$m and $h = 100\ \mu$m). Time is indicated in milliseconds and $t = 0$ matches the time when the neck breaks up. Gravity is pointing downward. The injection system is case i sketched in (c). (b) Evolution of the bubble's diameter d divided by the height h as a function of the flow rate q for different injection conditions. The inset shows the corresponding evolution of the necking time τ_n as a function of q. (c) Schematics of the different injection systems (see the text for more details).

If the pressure difference δp between the reservoir and the surrounding medium is small, one gets the law for the gas pressure release

$$\delta p(t) = \delta p(0) e^{-t p_e / R_t V s} \tag{15}$$

and the corresponding volumetric gas flow rate q_g at the exit is simply

$$q_g = \frac{\delta p(0)}{R_t} e^{-t/\tau}. \tag{16}$$

The pressure release is similar to the electric discharge of a capacitor through a resistance with a characteristic time τ equal to $R_t V s / p_e$. The volume of air prior to the capillary's end thus acts as a capacitor that leads to an increase of the bubble size during its formation through an extra gas flow q_g. The bubble formation is more complex since boundary conditions and flow properties are time dependent. Indeed, P_e is linked to the fingertip or bubble curvature that depends on time but also on the surface tension that may be dynamic since surfactants are present and the interface area is subjected to a fast stretching. Also, the gas boundary layer sets up inside the glass capillary on a timescale h^2/ν_g, where ν_g is the cinematic viscosity, that might not be negligible as compared to the necking time during which the bubble is formed. For $h = 100\ \mu$m, this time is 0.63 ms and τ_n is 4 ms. However, this simple analogy is enough to rationalize the observed trends.

Three injection cases have been considered where the glass capillary length is kept constant and set to 22 mm. The first one, labeled i in Figs. 8(b) and 8(c), corresponds to the one used for oils. The glass syringe has a volume of 5 ml and is connected to the glass capillary through a cylindrical tube having an inner diameter of 810 μm and a length of 0.5 m via a needle having a Luer taper glued on a glass plate. As previously mentioned, the bubble's diameter is about nine times h at low flow

rates. For the second one, labeled ii [Fig. 8(c)], the cylindrical tube is replaced by a 6-m-long tube having an inner diameter of 100 μm. The hydrodynamic resistance of this tube is thus increased by about 360. In that way, the syringe volume is isolated from the rest of the injection system. The only volume that plays the role of a capacitor is the needle one, including the Luer taper and the glass capillary. This volume is 0.135 ml. The capacitance is thus decreased, leading to a faster discharge time τ and thus lower gas flow rate (16). As a consequence, the bubble size is around $7.8\times h$ for low flow rates, while the necking time is similar [Fig. 8(b), inset]. For the third case, labeled iii [Fig. 8(c)], the Luer taper is cut, leading to a reduced volume of 0.026 ml. Again, the size is further decreased, down to about $7.1\times h$ for low q, and τ_n remains the same. We note that this value is still larger than the one for oils, which is 4.5. If now a thinner rectangular tube is used, more precisely, for $h = 50$ μm, the bubble diameter for low flow rates is $7.2\times h$. In addition, the necking time is two times shorter that for $h = 100$ μm [Fig. 8(b), inset]. These features are in accordance with the experimental scaling laws found for oils (2) and (3).

We did not manage to evaluate the critical flow rate above which the neck is stabilized by the flow when a long tube is used. Indeed, this latter introduces a too high pressure loss, above the working range of this injection system. On the other hand, for the injection system i, a critical flow rate of (1000 ± 200) ml/h could be measured. This corresponds to a critical capillary number times the aspect ratio of 0.014 ± 0.003 to be compared with the estimation of 0.009 given by the empirical law found with oils [Fig. 6(a), inset]. In addition, we notice oscillations of the neck with large amplitude before it breaks, which might be the result of a combination of low inertia and compressibility (see movie S2 in Ref. [28]). The transition features seems peculiar for air and further investigations are required to fully map the step-foaming dynamics.

IV. CONCLUSION

A rectangular glass tube is an efficient tool for making emulsion droplets at one of its extremities as well as for observing the dynamics of emulsification. This allowed us to extensively quantify the role played by the fluid properties and the tube geometry on such a process. Three regimes of drop production are observed. In the first regime, drop formation results from a competition between interfacial tension and viscous dissipation. This regime is usually referred to as step emulsification. In that regime, the drop size is governed by an inflation mechanism linked to a characteristic timescale of breakup, a necking time, and the flow rate of the dispersed phase. The necking time experiences a strong increase for an aspect ratio of the rectangular tube smaller than 2.5. This slower dynamics is attributed to a hindrance of the counterflow of the continuous liquid due to the drop itself during its formation. As a consequence, larger drops are formed for small aspect ratios. A semiempirical law of the drop size as a function of the flow rate, the liquid properties, and the tube dimensions for $w/h > 2.5$ is given. Above a critical capillary number, the necking of the liquid finger is stopped and a quasistatic shape takes place. Such a shape is well accounted for by a model based on a Hele-Shaw flow for an inner viscosity larger than 5 mPa s. In this model, the viscous pressure drop balances the capillary pressure variation linked to the shape of the interface between the two liquids. However, a more complete model is needed to take into account the flow in the continuous phase. Indeed, the critical capillary number above which the meniscus adopts a quasistatic shape is shown to be a function of the viscosity ratio. In that regime, the drops are then formed when other forces come into play, like gravity or shear if the continuous phase is under stirring. Then, by increasing the flow rate, and thus inertia, the drop formation undergoes a classical dripping to the jetting transition where the capillary instability becomes convective. A few experiments have been performed with air as the dispersed phase. While sharing common features with the emulsification process, the dynamics of bubble formation does not match exactly with the droplet one. First, for a given aspect ratio of the tube, the bubble size is about twice as large. Then the necking time is found to be almost three times larger than expected with an immiscible liquid. Finally, the transition between the first two regimes occurs at a higher capillary number. These

preliminary results thus present the opportunity for interesting future work on such a process when a compressible fluid is used.

ACKNOWLEDGMENT

This work was supported by a public grant overseen by the French National Research Agency as part of the Investissements d'Avenir program (Reference No. ANR-10-NANO-02).

[1] P.-G. de Gennes, F. Brochard-Wyart, and D. Quéré, *Capillarity and Wetting Phenomena: Drops, Bubbles, Pearls, Waves* (Springer, Berlin, 2004).
[2] J. B. Fournier and A. M. Cazabat, Tears of wine, Europhys. Lett. **20**, 517 (1992).
[3] J. Eggers and E. Villermaux, Physics of liquid jets, Rep. Prog. Phys. **71**, 036601 (2008).
[4] J. Roof, Snap-off of oil droplets in water-wet pores, Soc. Petrol. Eng. J. **10**, 85 (1970).
[5] R. Lenormand, C. Zarcone, and A. Sarr, Mechanisms of the displacement of one fluid by another in a network of capillary ducts, J. Fluid Mech. **135**, 337 (1983).
[6] T. Nakashima, M. Shimizu, and M. Kukizaki, Particle control of emulsion by membrane emulsification and its applications, Adv. Drug Delivery Rev. **45**, 47 (2000).
[7] S. M. Joscelyne and G. Tragardh, Membrane emulsification—A literature review, J. Membr. Sci. **169**, 107 (2000).
[8] G. T. Vladisavljevic and R. A. Williams, Recent developments in manufacturing emulsions and particulate products using membranes, Adv. Colloid Interface Sci. **113**, 1 (2005).
[9] T. Kawakatsu, Y. Kikuchi, and M. Nakajima, Regular-sized cell creation in microchannel emulsification by visual microprocessing method, J. Am. Oil Chem. Soc. **74**, 317 (1997).
[10] G. T. Vladisavljevic, I. Kobayashi, and M. Nakajima, Production of uniform droplets using membrane, microchannel and microfluidic emulsification devices, Microfluid. Nanofluid. **13**, 151 (2012).
[11] I. Kobayashi, M. Nakajima, K. Chun, Y. Kikuchi, and H. Fukita, Silicon array of elongated through-holes for monodisperse emulsion droplets, AIChE J. **48**, 1639 (2002).
[12] C. Priest, S. Herminghaus, and R. Seemann, Controlled electrocoalescence in microfluidics: Targeting a single lamella, Appl. Phys. Lett. **89**, 134101 (2006).
[13] F. Malloggi, N. Pannacci, R. Attia, F. Monti, P. Mary, H. Willaime, P. Tabeling, B. Cabane, and P. Poncet, Monodisperse colloids synthesized with nanofluidic technology, Langmuir **26**, 2369 (2010).
[14] R. Dangla, S. C. Kayi, and C. N. Baroud, Droplet microfluidics driven by gradients of confinement, Proc. Natl. Acad. Sci. USA **110**, 853 (2013).
[15] K. van Dijke, G. Veldhuis, K. Schroen, and R. Boom, Parallelized edge-based droplet generation (edge) devices, Lab Chip **9**, 2824 (2009).
[16] E. Amstad, M. Chemama, M. Eggersdorfer, L. R. Arriaga, M. P. Brenner, and D. A. Weitz, Robust scalable high throughput production of monodisperse drops, Lab Chip **16**, 4163 (2016).
[17] A. G. Håti, T. R. Szymborski, M. Steinacher, and E. Amstad, Production of monodisperse drops from viscous fluids, Lab Chip **18**, 648 (2018).
[18] M. Stoffel, S. Wahl, E. Lorenceau, R. Höhler, B. Mercier, and D. E. Angelescu, Bubble Production Mechanism in a Microfluidic Foam Generator, Phys. Rev. Lett. **108**, 198302 (2012).
[19] N. Mittal, C. Cohen, J. Bibette, and N. Bremond, Dynamics of step-emulsification: From a single to a collection of emulsion droplet generators, Phys. Fluids **26**, 082109 (2014).
[20] I. Kobayashi, Y. Wada, K. Uemura, and M. Nakajima, Microchannel emulsification for mass production of uniform fine droplets: Integration of microchannel arrays on a chip, Microfluid. Nanofluid. **8**, 255 (2010).
[21] A. B. Theberge, F. Courtois, Y. Schaerli, M. Fischlechner, C. Abell, F. Hollfelder, and W. T. S. Huck, Microdroplets in microfluidics: An evolving platform for discoveries in chemistry and biology, Angew. Chem. Int. Ed. **49**, 5846 (2010).
[22] J.-T. Wang, J. Wang, and J.-J. Han, Fabrication of advanced particles and particle-based materials assisted by droplet-based microfluidics, Small **7**, 1728 (2011).

[23] P. Gonzalez-Tello, F. Camacho, and G. Blazquez, Density and viscosity of concentrated aqueous solutions of polyethylene glycol, J. Chem. Eng. Data **39**, 611 (1994).
[24] C. Cohen, R. Giles, V. Sergeyeva, N. Mittal, P. Tabeling, D. Zerrouki, J. Baudry, J. Bibette, and N. Bremond, Parallelised production of fine and calibrated emulsions by coupling flow-focusing technique and partial wetting phenomenon, Microfluid. Nanofluid. **17**, 959 (2014).
[25] T. Kawakatsu, G. Tragardh, C. Tragardh, M. Nakajima, N. Oda, and T. Yonemoto, The effect of the hydrophobicity of microchannels and components in water and oil phases on droplet formation in microchannel water-in-oil emulsification, Colloids Surf. A **179**, 29 (2001).
[26] M. L. Eggersdorfer, H. Seybold, A. Ofner, D. A. Weitz, and A. Studart, Wetting controls of droplet formation in step emulsification, Proc. Natl. Acad. Sci. USA **115**, 9479 (2018).
[27] K. Schroën, M. Ferrando, S. de Lamo-Castellví, S. Sahin, and C. Güell, Linking findings in microfluidics to membrane emulsification process design: The importance of wettability and component interactions with interfaces, Membranes **6**, 26 (2016).
[28] See Supplemental Material at http://link.aps.org/supplemental/10.1103/PhysRevFluids.4.073602 for visualization of the nonwetting condition of oils on glass surface as well as movies showing drop or bubble formation.
[29] C. W. Park and G. M. Homsy, Two-phase displacement in Hele Shaw cells: Theory, J. Fluid Mech. **139**, 291 (1984).
[30] P. Garstecki, H. A. Stone, and G. M. Whitesides, Mechanism for Flow-Rate Controlled Breakup in Confined Geometries: A Route to Monodisperse Emulsions, Phys. Rev. Lett. **94**, 164501 (2005).
[31] B. Dollet, W. van Hoeve, J. P. Raven, P. Marmottant, and M. Versluis, Role of the Channel Geometry on the Bubble Pinch-off in Flow-Focusing Devices, Phys. Rev. Lett. **100**, 034504 (2008).
[32] R. Dangla, E. Fradet, Y. Lopez, and C. N. Baroud, The physical mechanisms of step emulsification, J. Phys. D **46**, 114003 (2013).
[33] K. van Dijke, I. Kobayashi, K. Schroen, K. Uemura, M. Nakajima, and R. Boom, Effect of viscosities of dispersed and continuous phases in microchannel oil-in-water emulsification, Microfluid. Nanofluid. **9**, 77 (2010).
[34] Z. Li, A. M. Leshansky, L. M. Pismen, and P. Tabeling, Step-emulsification in a microfluidic device, Lab Chip **15**, 1023 (2015).
[35] S. Barkley, E. R. Weeks, and K. Dalnoki-Veress, Snap-off production of monodisperse droplets, Eur. Phys. J. E **38**, 138 (2015).
[36] S. Barkley, S. J. Scarfe, E. R. Weeks, and K. Dalnoki-Veress, Predicting the size of droplets produced through laplace pressure induced snap-off, Soft Matter **12**, 7398 (2016).
[37] C. Clanet and J. C. Lasheras, Transition from dripping to jetting, J. Fluid Mech. **383**, 307 (1999).
[38] H. N. Oguz and A. Prosperetti, Dynamics of bubble growth and detachment from a needle, J. Fluid Mech. **257**, 111 (1993).